EFFECT OF WING PLANFORM SHAPE ON THE FLOW STRUCTURES OF AN INSECT-LIKE FLAPPING WING IN HOVER

N. Phillips, K. Knowles, N. J. Lawson
Cranfield University

Keywords: *flapping wing, insect flight, micro air vehicle, leading-edge vortex, particle image velocimetry*

Abstract

An experimental investigation of the effects of planform shape on the flow structures generated by an insect-like flapping wing in hover are presented. This was performed with application to flapping-wing micro air vehicles (FMAVs) in mind. Experiments were accomplished with a first-of-its-kind mechanical flapping-wing apparatus capable of reproducing a wide range of insect-like wing motions in air on the FMAV scale ($\sim 150mm$ wingspan). Four planform shapes with a constant area and aspect ratio of ~ 6 were considered: 'reverse-ellipse', rectangle, 'four-ellipse', ellipse. Particle image velocimetry (PIV) flowfield measurements of the entire volume from $18\% - 117\%$ span were performed on each planform at the mid-stroke position in an insect-like flapping cycle operating at $15Hz$ (giving a mean Reynolds number of $Re = \sim 13500$). Results revealed that the flow structures produced by each planform shape were very similar, and all exhibited a pair of leading-edge vortices (LEVs) of similar strength, and a distinct tip vortex. One of these leading-edge vortices was located right at the wing leading edge extending almost all the way down the span (secondary LEV), and the other more aft vortex (primary LEV) extended from the root and appeared to break down at around mid-span. Both vortices had the same sense with a positive z-wise vorticity (z axis points towards wingtip). The only significant planform effect was that a forward-swept leading edge impedes the formation of the primary LEV towards the root, and possibly shifts the primary vortex breakdown location towards the tip.

Nomenclature

AR = aspect ratio $(2r^2/s)$
$\bar{c}$ = mean chord length (s/r), m
f = flapping frequency, Hz
Q = Q criterion $((\| \Omega \|^2 - \| S \|^2)/2 > 0)$
r = length of one wing from root to tip, m
Re = mean Reynolds number $(\bar{V}_{tip}\bar{c}/\nu)$
s = planform area of one wing, m^2
S = antisymmetric part of ∇v
T = flapping period $(1/f)$, s
∇v = velocity gradient tensor
$\bar{V}_{tip}$ = mean wingtip speed, m/s
x = forward axis fixed to wing
y = vertical axis fixed to wing
z = lateral axis fixed to wing
X = forward axis fixed to insect body (see Fig. 1)
Y = vertical axis fixed to insect body (see Fig. 1)
Z = lateral axis fixed to insect body (see Fig. 1)
α = angle-of-attack, deg (see Fig. 1)
α_{mid} = angle-of-attack at mid-stroke, deg
θ = plunge angle, deg (see Fig. 1)
Θ = plunge amplitude, deg
ν = kinematic viscosity, m^2/s
ϕ = stroke angle, deg (see Fig. 1)
Φ = stroke amplitude, deg
Ω = symmetric part of ∇v

1 Introduction

An autonomous airborne system that can operate indoors would be useful for many applications including indoor reconnaissance, search and rescue, and inspection in hazardous areas. Currently, no such system exists. Autonomous unmanned air vehicles (UAVs) and micro air vehicles (MAVs) including fixed- and rotary-wing MAVs exist for outdoor use, however, a suitable system for indoor use has yet to be developed. This is because the requirements for this environment are extremely challenging, as they include high energy efficiency, and the abilities to operate at low flying speeds, sustain hover, and perform complex manoeuvres in confined spaces. As discussed in [1], the type of MAV that would best meet these requirements would be a flapping-wing micro air vehicle (FMAV) which mimics the flight of two-winged insects (Diptera). Insects are seen in nature to possess the remarkable abilities to sustain hover and perform rapid and complex manoeuvres in confined spaces. In addition, this mode of flight is apparently efficient at low speeds [2] and is not susceptible to wall proximity effects as rotary-wing MAVs are.

A hindrance in the development of FMAVs is the limited understanding of various aspects of insect-like flapping-wing aerodynamics. This has prompted the need for further experimental studies on the subject. One aspect that is relatively unexplored is wing planform shape effects. Usherwood & Ellington [3] varied leading-edge detail (thickness and serration), twist and camber for a model wing of a hawkmoth at $Re = 8071$, and measured aerodynamic forces and performed flow visualisation. This was done, however, with the same wing planform, and was a study on wing form and detail rather than planform shape. Heathcote and his colleagues varied chordwise [4] and later spanwise flexibility [5] on a plunging wing, but again, different planform shapes were unexplored as it was a study focusing on flexibility. Lu et al. [6] appear to have performed the only experimental study in which wing planform shape was explored. In their experiments they focused on the Reynolds number range of $160 - 3200$, and studied a fruitfly planform shape and a number of rectangular planforms with rounded tips of different aspect ratios. They observed the resulting effects on the formation of dual leading-edge vortices with dye flow visualisation and some particle image velocimetry (PIV) measurements. On the analytical side, the work of Ansari et al. [7] is the most extensive published exploration of wing geometry effects. They used an analytical model to vary geometric parameters systematically and observe the effects on lift, lift-to-drag and lift-to-torque ratios.

The aim of the present work was to explore experimentally the effects of changing planform shape on an insect-like flapping wing in hover, particularly at a Reynolds number more relevant to FMAVs (Re on the order of 10^4). The paper begins with the relevant background on insect flight and aerodynamic mechanisms (Section 2), followed by the aims and objectives of the present study (Section 3). An explanation of the experimental apparatus and setup is then given (Section 4) along with the experimental procedure (Section 5). The routine used in the data processing is then described (Section 6) followed by an uncertainty analysis (Section 7). Finally, results are presented and discussed (Section 8) as well as conclusions and future work (Section 9).

2 Insect Flight

2.1 Kinematics

The motion of an insect's wing can be broken down into four parts: downstroke, supination, upstroke and pronation (Figure 1). Starting with the downstroke, this is the translation of the wing at a relatively constant angle of attack from its most aft and dorsal position to its most forward and ventral position. At the end of the downstroke supination occurs, which is when the wing rapidly comes to a stop and reverses its direction and angle of attack so that the wing's underside becomes the topside for the subsequent half stroke. The wing then translates with a relatively constant angle of attack back to its most aft and dorsal position, which is referred to as

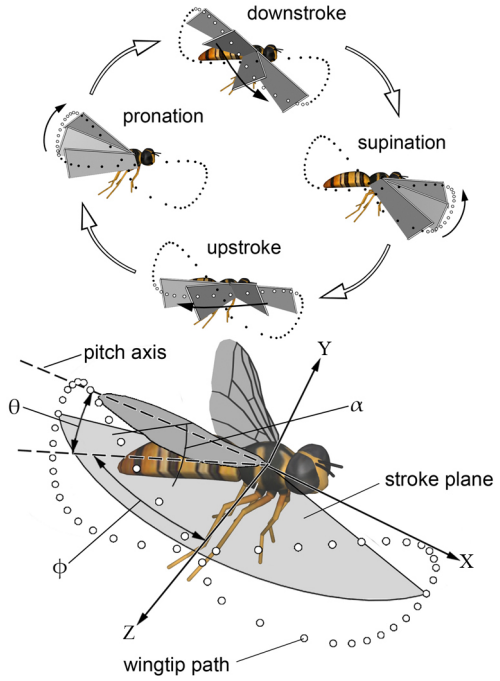

Fig. 1 Flapping cycle (top), definition of kinematic parameters (bottom)

the upstroke. Finally, at the end of the upstroke, the wing pronates when the wing again rapidly comes to a stop and reverses its direction and angle-of-attack. Pronation and supination can be advanced or delayed by insects relative to stroke reversal to modulate aerodynamic forces [8]. The flapping frequency (f) of insect wings ranges from $5-200Hz$, and the path that the wingtip traces takes the form of irregular, self intersecting shapes typically resembling a figure-of-eight.

An insect's wing motion is composed of three separate motions: sweeping (fore and aft), plunging (up and down) and pitching (angle-of-attack variation). The position of the wing at any given moment is defined relative to the stroke plane (Figure 1). After Willmott & Ellington [9], the angle from the Z (lateral) axis to the projection of the wing's longitudinal axis (pitch axis) onto the stroke plane is the stroke angle ϕ, the angle between the minimum and maximum stroke angles is the stroke amplitude Φ, and the plunge angle θ is the position of the wing's longitudinal axis out of the stroke plane. In addition, the angle between the minimum and maximum plunge angles is the plunge amplitude Θ and the wing's geometric angle of attack relative to the stroke plane is the pitch angle α, with α_{mid} referring to the angle of attack at mid-stroke. Another kinematic parameter that should be mentioned is rotation phase, which describes the timing of pitch reversal with stroke reversal. Here it is defined as a percentage of the flapping period T, where a positive sign implies that pitching begins early whereas a negative sign indicates that pitching is delayed. For example, at a $20Hz$ flapping frequency, a rotation phase of 5% means that the wing begins pitching early so that it reaches a 90° angle of attack $2.5ms$ before reaching the end of the stroke.

2.2 Aerodynamic Mechanisms

An insect's ability to produce lift values beyond predictions from steady state theory is a result of several aerodynamic mechanisms. A number of these will be described here, including the leading-edge vortex (LEV) and spanwise flow. A detailed discussion on aerodynamic mechanisms relevant to insects may be found elsewhere [10, 11].

The most important aerodynamic mechanism relevant to insects is the leading-edge vortex (LEV), which was observed to form on the wings of a real hawkmoth and a mechanical model of a hawkmoth (the 'flapper') by Ellington and his colleagues [12]. It is a conical, root-to-tip spiralling vortex formed at the leading edge of a wing travelling at a high angle of attack. It acts to augment lift by increasing the flow velocity over the top surface of the wing. Experiments by Ellington and his colleagues revealed the existence of a spanwise flow through the core of the LEV which occurs as a result of a pressure gradient from root to tip [12]. The mechanism was confirmed in computational studies by Wilkins [11, 13]. The LEV starts off small at the root and grows in size and strength towards the tip because of the increase in wing tangential velocity seen along the span from root to tip. The higher flow speeds (and hence lower pressures) near the wingtip induce a flow from the weaker (and relatively higher pressure) wing root end of

the LEV. It was suggested by Ellington that this spanwise flow stabilises the LEV (which would normally rapidly grow in size and be shed into the wake) and keeps it attached by transporting vorticity from the LEV into the tip vortex. This has been confirmed in CFD studies performed by Wilkins [11, 13] who observed that on a two-dimensional translating wing, the LEV forms and sheds within the first three chord lengths of travel (when $Re > 25$), whereas a three-dimensional rotating wing (at low to moderate aspect ratio) forms an attached and stable LEV even at higher Reynolds numbers (Re of the order of 10^4). In addition, experimental studies have shown that the LEV is stable in general for revolving wings of low to moderate aspect ratio [3, 14].

3 Aims & Objectives

The aim of the present study is to observe and understand the effects of planform shape on the flow generated by an insect-like flapping wing in hover at the FMAV scale. Of particular interest is the formation of the LEV and changes to its characteristics between different planform shapes.

4 Experimental Apparatus & Setup

4.1 'Flapperatus'

The mechanical flapper apparatus (the 'flapperatus') pictured in Figure 2, enables an insect-like wing to be flapped with three controllable degrees of freedom (sweeping, plunging and pitching). It operates in air on the FMAV scale ($\sim$ 150mm wingspan) so that it experiences the true flow conditions that a real FMAV would experience. Variable flapping-wing kinematics up to a 20Hz flapping frequency are produced using a patent-pending, three-degree-of-freedom $3-\underline{R}RR$ parallel spherical mechanism. The mechanism has three concentric drive shafts which are each coupled to servo motor via $1:1$ cable drive. In addition, an encoder is mounted on each drive shaft so that the time-history of the actual flapping kinematics can be recovered. The entire apparatus is mounted on a traverse which permits

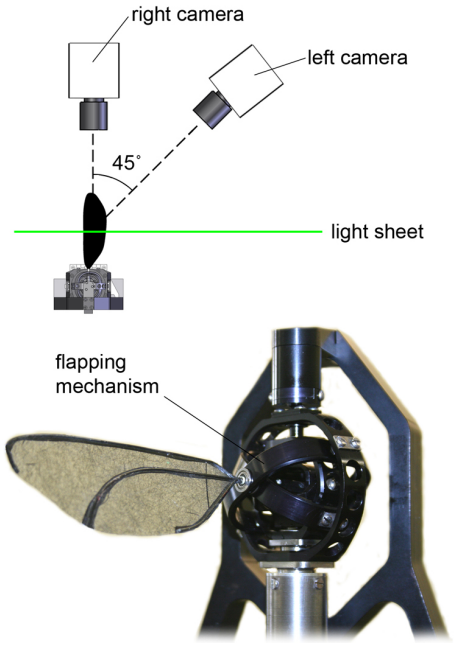

Fig. 2 PIV setup (top), flapperatus flapping mechanism (bottom)

measurement at different spanwise locations via translating the wing relative to the measurement plane. The flapperatus, and its flapping mechanism in particular, are described in greater detail elsewhere [15, 16].

For the present experiments, the flapperatus was placed inside an hexagonal test chamber designed to isolate the experiment from outside disturbances and contain the seeding, whilst minimising wall interference effects. Inside the chamber the flapping wing was positioned over 15, 6 and 13 wing lengths (r) from the walls, ceiling and floor respectively.

4.2 PIV Setup

The PIV system utilised an angular set-up, rather than a translational set-up due to its greater out-of-plane accuracy [17, 18]. Here, the cameras were oriented as illustrated in Figure 3 with the right camera viewing the measurement plane straight-on, and the left camera viewing at 45° from the normal with the CCD tilted with respect to the lens according to the Scheimpflug condition [19]. The area viewed was approximately $120 \times 120mm^2$, and the cameras used

were two FASTCAM-ultima APX high-speed cameras with a resolution of $1024 \times 1024 px^2$. A $60mm$ lens at an $f\#$ of 2.8, and a $105mm$ lens at an $f\#$ of 4 were used for the right and left cameras respectively. The laser light sheet was created with light sheet optics and a New Wave Research Gemini Nd:YAG double pulsed laser with a wavelength of 532 nm. The seeding used was smoke generated from a smoke machine using global mix smoke fluid by Le Maitre.

4.3 Wing Designs

The wing planform shapes used in the present experiment included a 'reverse-ellipse', rectangle, 'four-ellipse', and ellipse, as illustrated in Figure 3. Here, the 'four-ellipse' planform is from the wing design by Galiński & Żbikowski [20], which originated from the 'four-ellipse' of Pedersen [21]. Overall, these shapes encompass a number of geometric variations including area distribution, leading and trailing edge sweep, and tip width.

All shapes had approximately the same mean chord length ($\bar{c}$), planform area (s), and length (r), as indicated in Figure 4. This resulted in a constant aspect ratio (AR) between all planforms of approximately 6. It should be noted here that the reverse-ellipse planform had a slightly larger area due to the interface between the spar and the wing near the root section. In addition, for all planforms the pitch axis was placed at the quarter-chord of the maximum chord.

To minimise effects due to flexibility, the wings were made as stiff as possible. This was accomplished by sandwiching a $2mm$ diameter carbon-fibre rod between two $\sim 0.25mm$ thick carbon-fibre sheets. When mounted on the flapping mechanism, the root of each wing measured $24mm$ from the centre of rotation.

5 Experimental Procedure

The first step in the experimental procedure used for each wing planform was releasing smoke into the test chamber and then waiting four minutes until beginning the experiment. As will be described in Section 7, this 'settle time' was observed to be appropriate to allow the seeder-induced flow to reduce to an acceptable level, and for the seeding density to become uniform. After this 'settle time', the flapperatus was ramped up to a 15Hz flapping frequency with the flapping kinematics illustrated in Figure 4, which had a stroke amplitude, plunge amplitude, angle-of-attack at mid-stroke and rotation phase of 131.7°, 1.2°, 45.2°, and 6% respectively (where the definitions of these parameters are as described in Section 2). Once the flapperatus reached its desired flapping frequency, 10 seconds (150 flapping cycles) were allowed to elapse, which was assumed to be sufficient to surpass any start-up effects. Next, starting from approximately 18% span where % span is defined from the root of the wing, 15 image pairs (for both cameras) were acquired at mid-stroke ($\phi = 0°$) for each of 81 spanwise locations extending up to 117% span, and spaced $1mm$ apart. The end result was 2430 image pairs between the two cameras. As described in Section 4.1, changing the measurement position is accomplished by traversing the flappera-

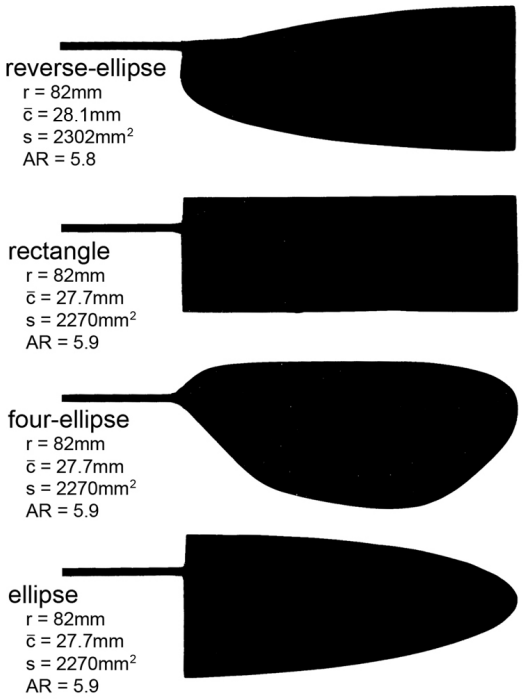

Fig. 3 Wing planforms

tus with respect to the measurement plane. Here the flapperatus was traversed in $1mm$ increments between measurements, where 40 flapping periods were allowed to elapse following the arrival at a new measurement position before acquiring image pairs. The average and peak traversing speeds in this case were 0.002% and 0.01% of the mean wingtip speed ($7.4m/s$) respectively. Nevertheless, to verify that the act of traversing the flapperatus in this manner did not alter the flow, measurements taken with traversing were compared to measurements with no traversing for the same spanwise measurement location. The resulting vector maps showed no differences in the flowfield.

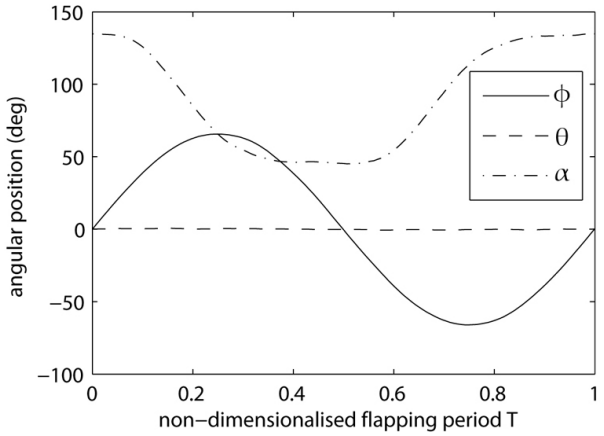

Fig. 4 Flapping kinematics; $f = 15$Hz; $\Phi = 131.7°$; $\Theta = 1.2°$; $\alpha_{mid} = 45.2°$; rotation phase $= 6\%$

In acquiring the image pairs, a pulse separation of $30\mu s$ was used, which was selected such that the maximum out-of-plane particle image displacement was less than or equal to one quarter of the thickness of the laser light sheet (given to be optimal in [22]) which was approximately $1mm$ thick. Here the expected out-of-plane velocity was the mean wingtip speed ($7.4m/s$), as the peak spanwise flow has consistently been reported to be comparable to this speed [11, 12, 23, 24].

6 Data Processing

Before image pairs were cross-correlated, reflections on the wing and in the background were removed by averaging the multiple samples of images taken at a given spanwise location for each exposure, and then subtracting these averages from each sample at the same measurement location. Processing was performed with an FFT-based cross-correlation algorithm with a Gaussian peak fit to locate correlation peaks to within sub-pixel resolution. An initial interrogation window size of 32×32 px^2 was employed, which progressed to a final interrogation window size of 16×16 px^2 with two passes and a 50% overlap. Deformed interrogation windows were also used which increases the number of matched particles and the signal-to-noise ratio. Between passes from the initial to final interrogation window size, the median filter proposed by Westerweel [25] was utilised to locate spurious vectors and replace them by interpolation. The resulting vector maps for a given measurement location were then averaged.

Kinematic data obtained from the drive shaft encoders were used to determine the actual wing speeds at the measurement point. These were then used to convert the measured vectors from laboratory coordinates to wing coordinates (vectors with respect to the wing). To identify vortical structures in the flow, the data were analysed using the Q criterion by Hunt et al. [26]. This criterion identifies vortices as areas where the second invariant Q, of the rate of deformation tensor ∇v is positive, where Q can be written as $Q = (\| \Omega \|^2 - \| S \|^2)/2$. Here Ω and S are the symmetric and antisymmetric parts of ∇v respectively. This decomposition can be thought of as separating the local fluid motion into strain and shear rates, which are lumped together in S, and rigid-body-like rotation rates which are grouped into Ω. Thus, if at a given location Ω dominates over S, then that region is a vortex since the local fluid motion will be dominated by rigid-body-like rotation.

The acquired image pairs were also used to reconstruct the instantaneous wing position, flexion and the local geometric angle of attack along the span. This was performed by locating the position of the leading and trailing edge in the many images taken along the span which essentially re-

veal $2D$ slices of the local wing position. Such a method was also employed by Poelma et al. [27].

7 Uncertainty Analysis

To ensure that measurements were not contaminated with flows generated in the act of filling the test chamber with smoke, a 'settle time' experiment was performed in which seeding was released (using a fixed burst length) and the resulting flow was measured using a pulse separation of $5ms$. After four minutes the flow settled to a level below $0.03m/s$ (approximately 0.4% of the mean wingtip speed), which was deemed to be sufficiently low that subsequent experiments would not be contaminated. In addition, a test was performed to ensure that no recirculation formed in the test chamber as a result of running the flapping-wing for a prolonged period of time. The flowfield was measured on the flapping-wing at set invervals at the same spanwise location over a period of seven minutes (longer than an experimental run). Results revealed that no recirculation was present as the velocity components did not drift over time.

Errors in the velocity field measurements were quantified using the approach described by Willert [28, 29], in which error is measured by processing particle image pairs where the particles have displaced by an amount that is known reliably. Using this approach, the flow was measured four minutes after a seeding burst (at which it was known that the flow velocity was below $0.03m/s$) using a short pulse separation of $4\mu s$. This short pulse separation in conjunction with a low flow velocity meant that the actual displacement of the particles between pulses was virtually zero. The captured image pairs were processed using the same method described in Section 6. The resulting displacements in conjunction with the pulse separation used in the experiment ($30\mu s$) revealed rms in-plane and out-of-plane errors of $0.19m/s$ and $0.23m/s$ respectively. These errors combine to a norm equal to 4% of the mean wingtip speed.

8 Results & Discussion

8.1 Wing Flexion

The measured angle-of-attack along the span for all planforms is shown in Figure 5, where the average angle along the span was 41.4°, 43.0°, 43.4°, and 45.7° for the reverse-ellipse, rectangle, four-ellipse, and ellipse planforms respectively. These angles are inversely proportional to the amount of wing area outboard. Here, the larger the area outboard, the greater the bending moment about the pitch axis in the pitch-down direction.

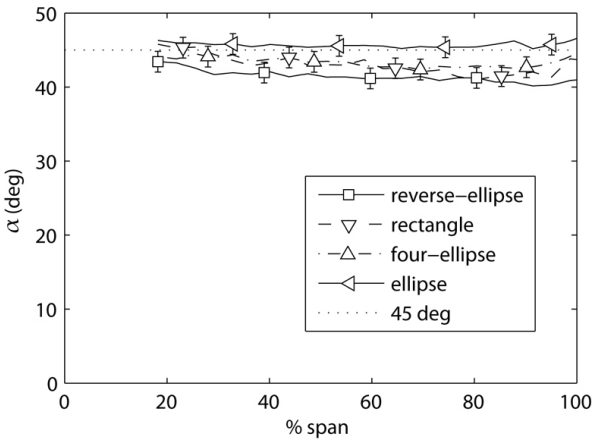

Fig. 5 Local angle-of-attack at mid-stroke, α_{mid}, along the wing span for all planforms

8.2 General Flow Structure

To aid in describing the flow structure we must first define a coordinate system. The origin is placed at the centre of rotation, where the x, y, and z axes point respectively forward (in the direction of wing rotation), vertically upwards, and towards the tip (collinear with the pitching axis). The form of the major flow structures for each of the wing geometries at mid-stroke is illustrated in Figure 6 which depicts the top, back and root views which look in the $-y$, x, and z directions respectively. Vortical structures are highlighted with transparent isosurfaces of Q (from the Q criterion as described in Section 6) normalised with respect to the maximum Q value. These are plotted for three different 'normalised Q' values: pur-

ple = 0.2, orange = 0.1, yellow = 0.05. In addition, the structure of the flow around these major vortices is illustrated with vectors in wing coordinates plotted on an isosurface of velocity magnitude (in laboratory coordinates) equal to the mean wingtip speed ($7.4m/s$).

Recall that Q provides a measure of the dominance of rotation rates over strain rates at a point in the fluid, where the more positive Q is the more rigid-body motions dominate, and the more negative Q is the more shearing motions dominate. Since vortex cores exhibit nearly rigid-body rotation, Q values will be largest in such regions because shear is virtually nonexistent. Thus, higher normalised Q values indicate regions where vortex cores are present.

It can be seen from the isosurfaces of normalised $Q = 0.2$ for all wing geometries, that two vortex core structures appear to be present along the leading edge. The reverse-ellipse planform differs slightly from the rest in this case as one vortex structure is present at the root which breaks into two vortices towards the tip. The more forward of these vortical structures is present right on the leading edge extending almost across the whole wingspan, while the other is the more well known LEV which is more aft of the leading edge and appears to break down at around mid-span. The more aft vortex will be referred to as the primary LEV, while the more forward will be termed the secondary LEV. Dual leading-edge vortices have been reported before by Lu et al. [6] who saw such structures on a flapping wing in a water tank for $Re \geq 640$.

To provide a comparison of the strengths of these leading-edge vortices, the upper portion of Figure 7 illustrates the normalised $Q = 0.2$ isosurfaces coloured with z-wise vorticity for the top views of the wing planforms. It can be seen that both of the leading-edge vortices have the same sense (this was also reported in [6]) and that their strengths across all planforms are very similar. Returning again to Figure 6, at the isosurfaces for the lower two normalised Q values, more of the vortex structures become visible. The moderate normalised Q level (0.1) is concentrated around the leading-edge vortices, and with addition of the low normalised Q level (0.05) the tip vortex for each wing planform becomes clear. The sense of each tip vortex is made visible by the velocity vectors showing a distinct spiralling motion. A conical region of vortical flow extending from the more aft primary LEV is also made visible on all wing planforms by the lower two normalised Q isosurfaces.

8.3 Vortex Breakdown

In all cases, the primary LEV starts off with a smaller diameter and with a higher Q value at the root. Progressing towards the tip it stays somewhat the same size and of similar strength until reaching a breakdown location where the Q value suddenly falls and the diameter rapidly expands as shown in the lower normalised Q isosurfaces. This is a classic indication of vortex breakdown (also known as vortex burst). Vortex breakdown occurs when a stagnation point is present on the vortex axis followed by a region of reversed flow [30]. This definition explains why such a breakdown occurs in this case, because the primary LEV which is spiralling towards the tip encounters root-ward flow originating from the tip vortex. Between these two competing flows a stagnation point is present which is the breakdown location. This view is supported by Liu et al. [31] who postulated that an adverse pressure gradient resulting from flow from the tip vortex is created above the wing surface which leads to vortex breakdown.

The sudden drop in the Q value beyond the apparent breakdown point for all planforms seen in Figure 6, implies that the vortex structure transitions from a rigid-body-like rotation to a state with comparatively higher strain rates. This makes sense in view of the fact that this vortex suddenly expands beyond the breakdown location, where by conservation of angular momentum the spiralling fluid with a tight radius from the root must decrease in angular velocity as the radius suddenly expands. Thus the rotation rates in the fluid go down with angular velocity and the strain rates become comparatively larger which means a lower Q value. For this reason, it is felt

that a sudden drop in Q value at this point is a good indicator of the vortex breakdown location.

An unexpected consequence of averaging multiple images obtained at a given measurement location is that the core of the primary LEV becomes visible. This is because the seeding particles (smoke) are slightly more dense than the fluid. In a vortical flow this means that in comparison to a fluid element, the smoke particles will have a larger centrifugal force (pulling the particle away from the centre of rotation) compared to the radial pressure gradient (pulling the particle towards the centre of rotation). The result is that the seeding density in the core of the LEV is less than elsewhere in the fluid. In a single exposure this lower level of seeding density in such a region is invisible, however, when multiple images for the same measurement location are averaged it becomes quite clear.

Figure 7 shows images averaged in the manner mentioned previously. These images were generated from averaging 15 samples of the first exposure at each of four spanwise locations (30.5%, 42.7%, 54.9%, 67.1%) straddling the breakdown region for each wing planform. For comparison, the same spanwise locations are also labeled on the isosurfaces of normalised $Q = 0.2$ coloured with z-wise vorticity. It can be seen for the rectangle, four-ellipse and ellipse planforms that inboard of the breakdown location the primary LEV is quite concentrated and grows only slightly from 30.5% to 42.7% span. The reverse-ellipse differs from this, where at 30.5% span the primary vortex core is barely visible, however, at 42.7% span it grows to a size comparable to that seen at the same spanwise location for the other planforms. Around the breakdown location at 54.9% span and beyond to 67.1% span, the core structures for all planforms are similar and appear to suddenly expand and become less distinct. This is in agreement with the conical vortex structures observed in the moderate and low normalised Q isosurfaces in Figure 6.

Vortex breakdown has been seen to occur in numerous experiments on insect-like flapping wings at Reynolds numbers of the order of 10^3 and above (see [6, 32, 33, 14]). CFD studies have also observed breakdown or hints of the occurrence of breakdown [31, 11]. It has been seen that breakdown begins around mid-stroke when the wing begins decelerating after which it is intensified [33, 14]. The location of breakdown appears to vary as it has been seen to occur at mid-span [33, 14] and two-thirds of the wing length [32]. The results presented are in agreement with previously observed trends as vortex bursting occurs here at mid-stroke around mid-span for all planforms tested at $Re =\sim 13500$.

8.4 Leading-Edge Sweep Effects

The observations in Figure 7 suggest that a forward-swept leading edge suppresses the formation of the primary LEV. Given that the normalised $Q = 0.2$ isosurface for this planform does not appear close to the root and the LEV's small structure seen in the averaged image at 30.5% span, it seems as though the primary LEV does not form until close to 30.5% span. In contrast, the primary LEV is quite visible inboard of 30.5% span for the other planform shapes. This effect is thought to be caused by the forward-swept leading edge having a free-stream velocity component towards the root, which appears to impede the formation and growth of the LEV. The forward-sweep on the leading edge of the reverse-ellipse planform varies in this case from root to tip. Towards the root the where the forward-sweep is greatest, the primary LEV is more affected and is even absent. As the forward sweep decreases towards the tip, a single leading edge vortical structure (no secondary LEV) forms which then appears to split into the primary and secondary LEV. The leading edge for this planform approaches a straight leading edge geometry towards the tip, and it appears as a consequence of this that the vortex structures towards the tip more resemble those seen on planforms with straight leading edges (rectangle and four-ellipse), where the primary vortex even breaks down around the same location. However, it appears as though the breakdown location on the reverse-ellipse is slightly further outboard than the rest, suggesting that a forward-swept leading

edge also shifts the vortex bursting location outboard.

An aft-swept leading edge (ellipse planform) appears to have no noticeable effect on the vortex structures when compared to the straight leading edge planforms. The vortex cores are of similar size across 30.5%-42.7% span as depicted in the averaged images in Figure 7, and the breakdown location appears to be the same.

8.5 Overall Planform Effect

It is apparent that, overall, the flow structures on all four planform shapes are very similar, despite the drastic differences in geometry. This implies that planform shape generally has little effect on the flow structure over the wing. This view has been supported elsewhere. Experiments by Lu et al. [6] who looked at the Reynolds number range $160 - 3200$, postulated that the effect of geometry was only slight, as they saw with dye visualisation that aspect ratio, and a curved leading edge geometry had little effect on the dual leading edge vortices that were formed. CFD studies by Wilkins [11] who tested the same ellipse, rectangle, and reverse-ellipse planforms (but with a smaller aspect ratio) reported little impact on the flow phenomenology for a constant aspect ratio. From the present results these conclusions have now been extended and verified at true FMAV-like conditions (in air, at Re of the order of 10^4, at the FMAV scale, with full flapping kinematics).

It is worth noting that although planform shape has little effect on the general flow structures, it has been seen computationally and analytically that it significantly impacts aerodynamic forces. Wilkins [11], who as previously mentioned computationally studied similar wing geometries, found lift coefficients between these planform shapes to be quite different. Here, the reverse-ellipse performed the best, followed by the rectangle and then the ellipse planform which performed the worst. Similarly, results from Ansari et al. [7], who analytically studied wing geometry effects (on the same wing geometries presented here), indicate that with the wing geometries used here the reverse and four-ellipse planform shapes are best and will produce comparable values of lift. This is followed by the rectangle and ellipse planform shapes which would perform the worst in terms of lift production.

9 Conclusions & Future Work

The full flowfield volume around an insect-like flapping wing at mid-stroke at the FMAV scale was measured and visualised for four different wing planform shapes of constant aspect ratio and planform area. In terms of geometry, the shapes used varied in distribution of area, leading- and trailing-edge sweep, and wing tip geometry. Despite the wide differences in wing geometries used, the general flow structures on all planform shapes were very similar. All shapes exhibited a pair of leading-edge vortices of similar strength, and a distinct tip vortex. One of these leading-edge vortices was located right at the wing leading edge extending almost all the way down the span (secondary LEV), and the other more aft (primary) LEV extended from the root and broke down at around mid-span. The only noticeable effect was that a forward-swept leading edge impedes the formation of the primary LEV towards the root, and possibly shifts the primary vortex breakdown location towards the tip. Future work will investigate the effect of planform shape on the mean lift generated, as although planform shape has little effect on the flow structures, it has been observed computationally and analytically to have significant effects on forces.

Acknowledgements

The authors would like to thank Professor Rafał Żbikowski for his guidance on data reduction and other contributions to the setup of this investigation; and Dr. Graham Stabler for his help and advice in the development of the experimental apparatus and the flapping wing designs.

References

[1] Żbikowski, R., "Flapping wing autonomous micro air vehicles: research programme outline," *Fourteenth International Conference on Unmanned Air Vehicle Systems*, Vol. Supplementary Papers, 1999, pp. 38.1–38.5.

[2] Woods, M. I., Henderson, J. F., and Lock, G. D., "Energy requirements for the flight of micro air vehicles," *The Aeronautical Journal*, Vol. 105, No. 1043, March 2001, pp. 135–149.

[3] Usherwood, J. R. and Ellington, C. P., "The aerodynamics of revolving wings I. Model hawkmoth wings," *Journal of Experimental Biology*, Vol. 205, 2002, pp. 1547–1564.

[4] Heathcote, S.and Gursul, I., "Flexible flapping airfoil propulsion at low Reynolds numbers," *AIAA Journal*, Vol. 45, 2007, pp. 1066–1078.

[5] Heathcote, S., Wang, Z., and Gursul, I., "Effect of spanwise flexibility on flapping wing propulsion," *Journal of Fluids and Structures*, Vol. 24, 2008, pp. 183–199.

[6] Lu, Y., Shen, G. X., and Lai, G. J., "Dual leading-edge vortices on flapping wings," *Journal of Experimental Biology*, Vol. 209, 2006, pp. 5005–5016.

[7] Ansari, S. A., Knowles, K., and Żbikowski, R., "Design study of insect-like flapping wings in the hover. Part II: effect of wing geometry," 2008, pp. 1976–1990.

[8] Dickinson, M. H., Lehmann, F.-O., and Sane, S. P., "Wing rotation and the aerodynamic basis of insect flight," *Science*, Vol. 284, No. 5422, 18 June 1999, pp. 1954–1960.

[9] Willmott, A. P. and Ellington, C. P., "The mechanics of flight in the hawkmoth manduca sexta: I. Kinematics of hovering and forward flight," *Journal of Experimental Biology*, Vol. 200, 1997, pp. 2705–2722.

[10] Ansari, S. A., *A nonlinear, unsteady, aerodynamic model for insect-like flapping wings in the hover with micro air vehicle applications*, Ph.D. thesis, Cranfield University (Shrivenham), September 2004.

[11] Wilkins, P. C., *Some unsteady aerodynamics relevant to insect-inspired flapping-wing micro air vehicles*, Ph.D. thesis, Cranfield University (Shrivenham), June 2008, http://hdl.handle.net/1826/2913.

[12] Ellington, C. P., van den Berg, C., Willmott, A. P., and Thomas, A. L. R., "Leading-edge vortices in insect flight," *Nature*, Vol. 384, 19/26 December 1996, pp. 626–630.

[13] Wilkins, P. C. and Knowles, K., "The leading-edge vortex and aerodynamics of insect-based flapping-wing micro air vehicles," *Aeronautical Journal*, Vol. 113, No.1143, 2009, pp. 253–262.

[14] Lentink, D. and Dickinson, M. H., "Rotational accelerations stabilize leading edge vortices on revolving fly wings," *Journal of Experimental Biology*, Vol. 212, 2009, pp. 2705–2719.

[15] Phillips, N. and Knowles, K., "Effect of flapping kinematics on the mean lift of an insect-like flapping wing," Submitted to *Proc. IMechE, Part G, Journal of Aerospace Engineering*.

[16] Phillips, N. and Knowles, K., "Progress in the development of an adjustable, insect-like flapping wing apparatus utilising a three degree-of-freedom parallel spherical mechanism," *International Powered Lift Conference*, Royal Aeronautical Society, London, July 2008.

[17] Lawson., N. J. and Wu, J., "Three-dimensional particle image velocimetry: error analysis of stereoscopic techniques," *Measurement Science and Technology*, Vol. 8, 1997, pp. 894–900.

[18] Prasad, A. K., "Stereoscopic particle image velocimetry," *Experiments in Fluids*, Vol. 29, 2000, pp. 103–116.

[19] Raffel, M., Willert, C., and Kompenhans, J., *Particle image velocimetry: a practical guide*, Springer, 1998.

[20] Galiński, C. and Żbikowski, R., "Materials challenges in the design of an insect-like flapping wing mechanism based on a four-bar linkage," *Materials & Design*, Vol. 28, No. 3, 2007, pp. 783–796.

[21] Pedersen, C. B., *An indicial-Polhamus model of aerodynamics of insect-like flapping wings in hover*, Ph.D. thesis, Cranfield University (Shrivenham), 17 June 2003.

[22] Keane, R. D. and Adrian, R. J., "Optimization of particle image velocimeters. Part II: Multiple pulsed systems," *Measurement Science and Technology*, Vol. 2, 1991, pp. 963–974.

[23] Ramasamy, M. and Leishman, J. G., "Phase-locked particle image velocimetry measure-

ments of a flapping wing," *Journal of Aircraft*, Vol. 43, No. 6, November-December 2006, pp. 1867–1875.

[24] Ansari, S. A., Phillips, N., Stabler, G., Wilkins, P. C., Żbikowski, R., and Knowles, K., "Experimental investigation of some aspects of insect-like flapping flight aerodynamics for application to micro air vehicles," *Experiments in Fluids*, Vol. 46, No.5, 2009, pp. 777–798.

[25] Westerweel, J., "Efficient detection of spurious vectors in particle image velocimetry data," *Experiments in Fluids*, Vol. 16, 1994, pp. 236–247.

[26] Hunt, J. C. R., Wray, A. A., and Moin, P., "Eddies, stream, and convergence zones in turbulent flows," *Center for Turbulence Research*, Vol. Report CTR-S88, 1988, pp. 193–208, Report CTR-S88.

[27] Poelma, C., Dickson, W. B., and Dickinson, M. H., "Time-resolved reconstruction of the full velocity field around a dynamically-scaled flapping wing," *Experiments in Fluids*, Vol. 41, 2006, pp. 213–225.

[28] Willert, C. E. and Gharib, M., "Digital particle image velocimetry," *Experiments in Fluids*, Vol. 10, 1991, pp. 181–193.

[29] Willert, C. E., "Stereoscopic digital particle image velocimetry for application in wind tunnel flows," *Measurement Science and Technology*, Vol. 8, 1997, pp. 1465–1479.

[30] Leibovich, S., "Vortex Stability and Breakdown: Survey and Extension," *AIAA Journal*, Vol. 22, No. 9, September 1984, pp. 1192–1206.

[31] Liu, H., Ellington, C. P., Kawachi, K., van den Berg, C., and Wilmott, A. P., "A Computational Fluid Dynamic Study of Hawkmoth Hovering," *Journal of Experimental Biology*, Vol. 201, 1998, pp. 461–477.

[32] van den Berg, C. and Ellington, C. P., "The Three-Dimensional Leading-Edge Vortex of a "Hovering" Model Hawkmoth," *Philosophical Transactions of the Royal Society of London Series B*, Vol. 352, No. 1351, 29 March 1997, pp. 329–340.

[33] Lu, Y. and Shen, G. X., "Three-dimensional flow structures and evolution of the leading-edge vortices on a flapping wing," *Journal of Experimental Biology*, Vol. 211, No. 8, 2008, pp. 1221–1230.

Contact Details

Primary Point of Contact

Nathan Phillips
Aeromechanical Systems Group
Cranfield University
Defence Academy of the UK
Shrivenham, SN6 8LA
email: n.phillips@cranfield.ac.uk

Coauthors

Professor Kevin Knowles
Aeromechanical Systems Group
Cranfield University
Defence Academy of the UK
Shrivenham, SN6 8LA
email: k.knowles@cranfield.ac.uk

Dr. Nicholas J. Lawson
Department of Aerospace Engineering
School of Engineering
Cranfield University
Bedfordshire, MK43 OAL
email: n.lawson@cranfield.ac.uk

Copyright Statement

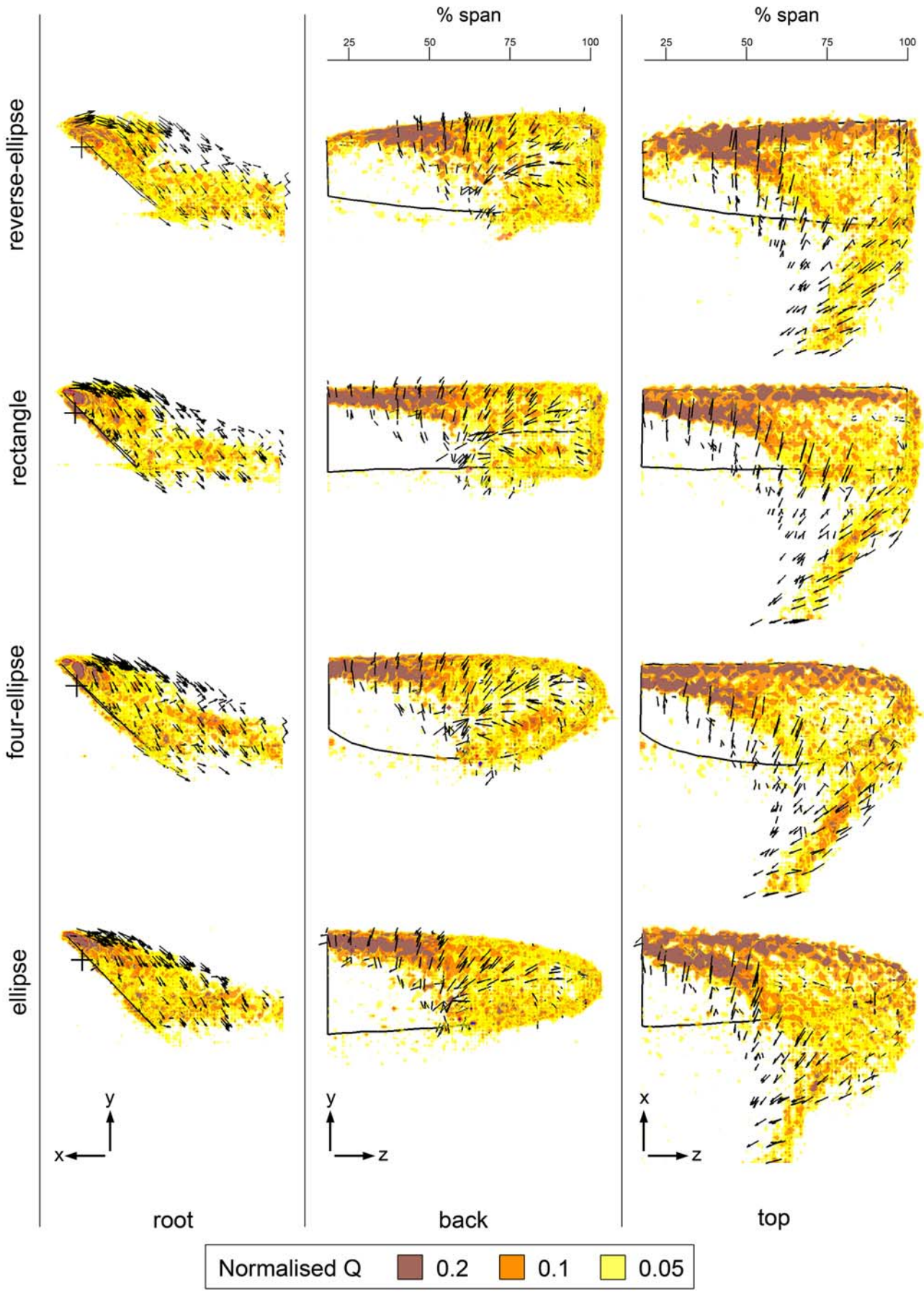

Fig. 6 3−view of flow around each planform shape at mid-stroke, showing primary leading-edge vortex breakdown at around mid-span; iso-surfaces are of constant normalised Q; x, y, z axes not placed at origin; wing planform only plotted outboard of 18% span

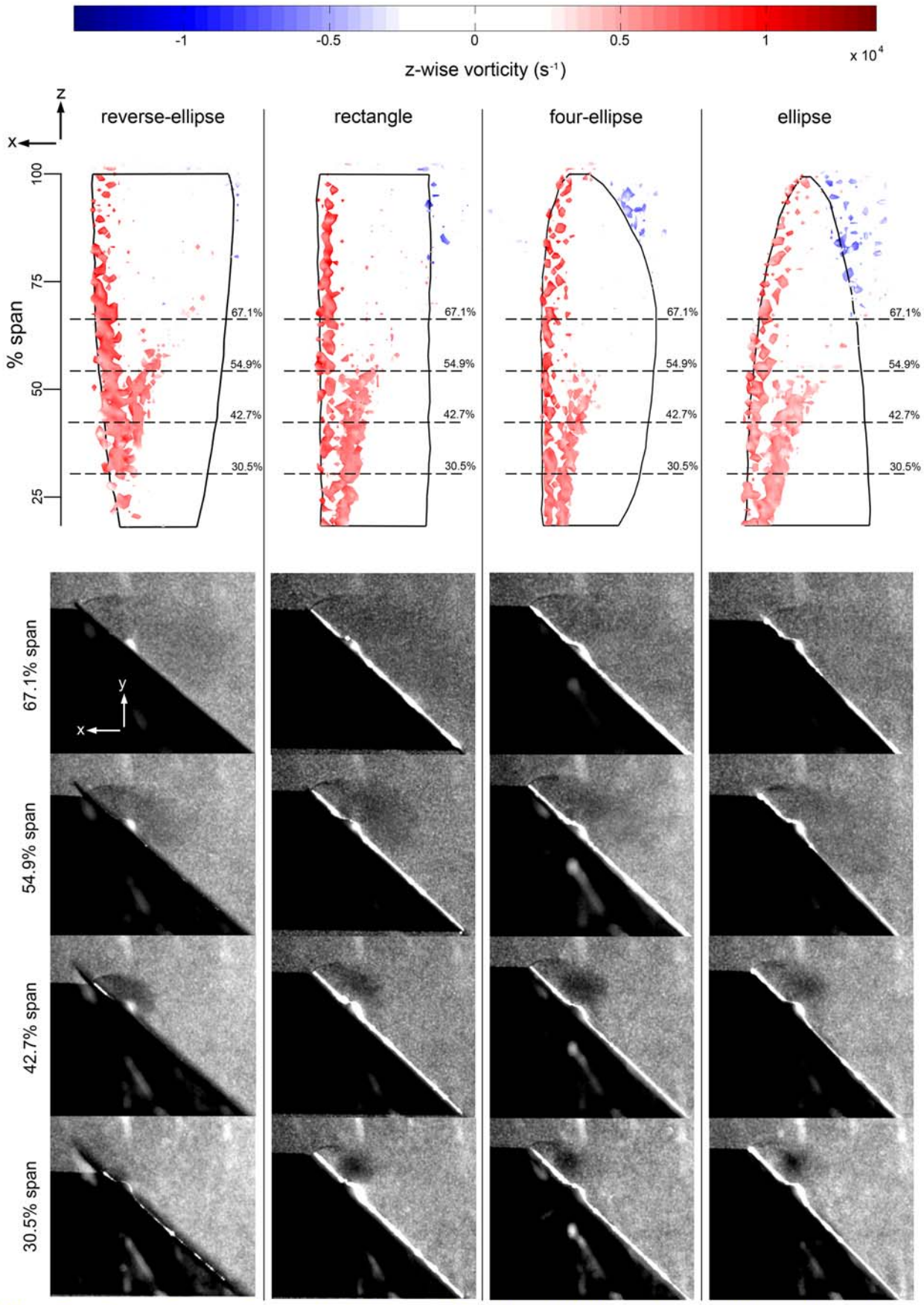

Fig. 7 Isosurfaces of normalised $Q = 0.2$ coloured with $z-$wise vorticity to show the sense of leading-edge vortices for each planform at mid-stroke (top); average of multiple image samples at various spanwise locations revealing a dark spot, which is the core of the primary leading-edge vortex (bottom); x, y, z not placed at origin; wing planform only plotted outboard of 18% span